Batteries

Weakly-Solvated and Co-Intercalation-Free Ether-Based Electrolytes Enhance the Low- Temperature and Fast-Charging Performance of LiFePO₄||Graphite Batteries

Ziwei Wang, Xuewei Gu, Jiacheng Zhu, Cong Zhong, Shiwei Xu, Suting Weng, Bowen Liu, Zhaoxiang Wang, Yejing Li,* Tao Cheng,* and Xuefeng Wang*

Abstract: Lithium-ion batteries (LIBs) employing lithium iron phosphate (LiFePO₄, LFP) cathodes and graphite (Gr) anodes are extensively utilized for energy storage applications because of their exceptional cycle life and inherent safety characteristics. However, sluggish desolvation kinetics and interfacial Li⁺ transport hinder their fast-charging capability and low-temperature performance, limiting broader applications. In this work, we propose a weakly solvating ether (WSE) electrolyte based on 2-methyl-tetrahydrofuran (2MT) as the main solvent. This electrolyte results in considerable steric hindrance, effectively preventing co-intercalation with Gr, while also providing a weak solvation capability for Li⁺ ions and facilitating rapid interfacial Li⁺ transport. WSE, formulated with 2MT and fluoroethylene carbonate (FEC) as a co-solvent, combines fast desolvation kinetics with an extremely low freezing point of −117.67 °C. This electrolyte induces the formation of a LiF-, Li₃N-, Li₂CO₃-, and Li₂O-rich solid electrolyte interphase (SEI) on the Gr anode, thereby enhancing low-temperature interfacial transport. Consequently, the Gr||Li half-cell and the LFP||Gr full cell with this WSE demonstrates excellent rate performance, stable cycling stability, and a high specific capacity at −30 °C while also delivering reliable power even at −60 °C. These results underscore the electrolyte's efficient desolvation process, stable SEI layer, and excellent compatibility with graphite, rendering it ideal for extreme-temperature applications.

Introduction

Lithium-ion batteries (LIBs) constitute a cornerstone of energy storage technology because of their high energy density, long lifespan, and environmental friendliness.[1–3] Among these, lithium iron phosphate (LiFePO₄, LFP)||graphite (Gr) LIBs not only dominate the energy storage sector but also occupy a larger share of the power battery market than layered oxide/Gr systems do.[4,5] However, their performance deteriorates significantly at low temperatures (< −10 °C)[5–9]

and high charge–discharge rates (>3C),[10–12] leading to severe capacity fade, large polarization, and lithium dendrite growth.[13–17] These limitations hinder their application in high-latitude regions, military equipment, and deep-space exploration.[13,16,17] The dramatic performance degradation of LFP||Gr LIBs at low temperatures and high rates is attributed primarily to slow reaction kinetics associated with desolvation processes and interfacial Li⁺ transport. This results in capacity loss and potential growth of lithium dendrites.[18–20] Addressing these challenges necessitates more stringent requirements for electrolyte design and optimization.

Conventional carbonate-based electrolytes, such as those containing ethylene carbonate (EC), are widely used in commercial LIBs because of their high dielectric constant, which facilitates lithium salt dissociation and enables the formation of a dense solid electrolyte interphase (SEI) on Gr anodes.[13,21,22] However, EC has a high melting point (36.4 °C), causing commercial electrolytes to solidify at temperatures below −20 °C. This significantly reduces the electrolyte conductivity and ionic transport efficiency.[23–25] Although linear carbonates such as ethyl methyl carbonate (EMC) exhibit low melting points (−50 °C) and viscosities (0.65 mPa·s), their strong coordination with Li⁺ results in high desolvation energy barriers (−245.9 kJ mol⁻¹).[26] Additionally, organic intermediates formed in the SEI further impede ionic transport at low temperatures.[26]

To address these challenges, researchers have explored weakly solvating electrolytes (WSEs), which exhibit low binding energies between Li⁺ and solvent molecules. This facilitates faster desolvation kinetics and interfacial Li⁺

[*] Z. Wang, J. Zhu, Dr. S. Xu, Dr. S. Weng, B. Liu, Prof. Z. Wang, Prof. X. Wang
Beijing National Laboratory for Condensed Matter Physics, Institute of Physics, Chinese Academy of Sciences, Beijing 100190, China
E-mail: wxf@iphy.ac.cn

Z. Wang, J. Zhu, Prof. Z. Wang, Prof. X. Wang
College of Materials Science and Opto-Electronic Technology, University of Chinese Academy of Sciences, Beijing 100049, China

X. Gu, Prof. T. Cheng
Institute of Functional Nano and Soft Materials, Soochow University, Suzhou 215123, China
E-mail: tcheng@suda.edu.cn

C. Zhong, Prof. Y. Li
State Key Laboratory of Advanced Metallurgy, School of Metallurgical and Ecological Engineering, University of Science and Technology Beijing, Beijing 100083, China
E-mail: liyejing@ustb.edu.cn

Additional supporting information can be found online in the Supporting Information section
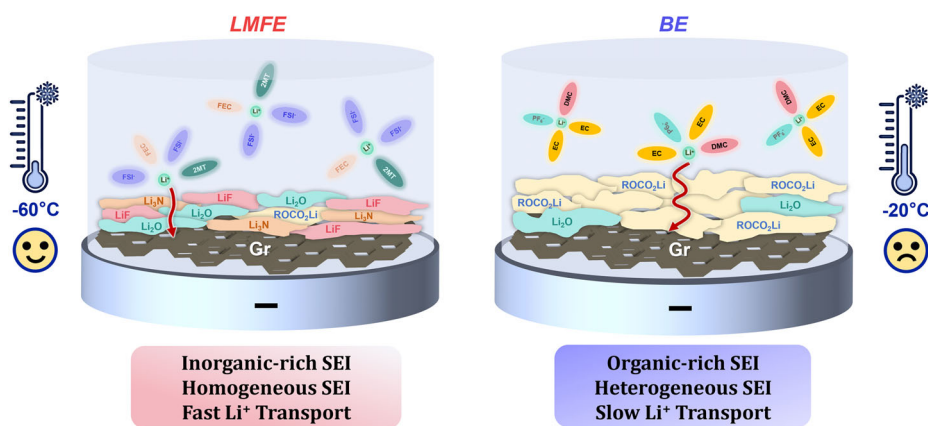
Figure 1. Schematic diagram of the desolvation process and interfacial Li$^+$ transport on the Gr anode with 1.5 M LiFSI /2MT:FEC (LMFE, left) and 1 M LiPF$_6$/EC:DMC (Base Electrolytes, BE, right).

transport under low-temperature conditions.[18,25,27] However, the practical application of WSEs faces significant challenges, particularly in terms of compatibility with Gr anodes. Ether solvents, which are commonly used in WSEs, often suffer from co-intercalation into the Gr layers, leading to structural damage and rapid capacity decay, as observed with tetrahydrofuran (THF).[28–31] This underscores the necessity of developing electrolytes that exhibit both low-temperature stability and compatibility with Gr, thereby ensuring robust lithium-ion battery performance under extreme conditions.

In this work, we propose a co-intercalation-free weakly-solvating electrolyte (LMFE) based on 2-methyl-tetrahydrofuran (2MT), which has an extremely low freezing point of − 117.67 °C. The LMFE formulation (1.5 M lithium bis(fluorosulfonyl)imide, LiFSI, in a 9:1 volumetric mixture of 2MT and FEC) ensures that the electrolyte remains liquid at temperatures below −60 °C, whereas conventional carbonate-based electrolytes solidify at −20 °C. A LiF-, Li$_3$N-, Li$_2$CO$_3$-, and Li$_2$O-rich SEI is formed on the Gr anode, thereby enhancing interfacial Li$^+$ transport (Figure 1). Consequently, the Gr‖Li half-cell with this electrolyte delivers a high reversible capacity of 244 mAh g^{-1} and a Coulombic efficiency of 98.31% at −30 °C. At a 5C charge rate, it provides a capacity of 288 mAh g^{-1}. Furthermore, the LFP‖Gr full cell maintains capacity retentions of 90.36% and 99.67% Coulombic efficiency after 300 cycles at −30 °C while also providing reliable power even at −60 °C. These results highlight the critical role of electrolyte solvent selection in enabling low desolvation barriers and high ionic conductivity, thereby improving the reaction kinetics and cycling stability under low-temperature and fast-charging conditions.

Results and Discussion

Choice of Solvent Weakly Binding with Li$^+$

To identify suitable solvents for weakly-solvating electrolytes (WSEs), the binding energies (E_B) between Li$^+$ and various solvents were calculated using density functional theory (DFT). Among the various ether/carbonate solvents and

diluent-type solvents, THF and 2MT exhibited notably weak E_B (Figure 2a) in the Li$^+$-(solvent)$_1$ complexes compared to the other solvents investigated (Table S1), which indicate that THF and 2MT are promising candidates for preparing weakly-solvating electrolytes. However, THF tends to co-intercalate into the Gr anode during cycling, showing a distinct voltage plateau at ~1.0 V and a low initial Coulombic efficiency (ICE) of 73.4% (Figure 2b), whereas 2MT avoids this issue, with a higher ICE of 96.3% at 0.1C. Additionally, the freezing point of 2MT is lower (−136 °C, Table S2) than that of THF (−108 °C, Table S2), which makes it more suitable for low-temperature applications. It is also more stable against Lewis acids than THF, enhancing the chemical stability of the electrolyte.[32] Furthermore, an additional advantage of 2MT is its renewable origin, as its synthetic precursor, 2-furaldehyde, is derived from agricultural waste such as corncobs and bagasse, making 2MT both cost-effective and widely available. Therefore, 2MT was ultimately selected as the main solvent for low-temperature LIBs.[33] To validate the weak solvation capability of 2MT, we formulated electrolytes using dimethoxyethane (DME)—a strongly solvating solvent—as a comparative benchmark. Comprehensive analyses, including density functional theory (DFT), radial distribution function (RDF), molecular dynamics (MD) simulations, Raman spectroscopy, and electrochemical characterization were conducted (Figures S1–S4).

With respect to the choice of salt, lithium bis(fluorosulfonyl)imide (LiFSI) was selected because of its superior solubility, dissociation properties, and film-forming capabilities.[1] Its concentration was determined by comparing the cycling performance of Li‖Li symmetric cells (plating and stripping for 1 mAh cm^{-2}) at −50 °C with different salt concentrations. As shown in Figure 2c, the electrolyte with 1.5 M LiFSI has the longest cycling life, which lasts for 330 h (Figure S5), whereas those with 1 M and 2 M LiFSI last for 298 h and 120 h, respectively. To compensate for the film-forming capability of 2MT, 10 vol% fluoroethylene carbonate (FEC) was added as a co-solvent, contributing to a stable interface against the lithium metal anode (Figure S6). This dual functionality ensures robust SEI formation while preserving the ultralow freezing point (−136 °C)
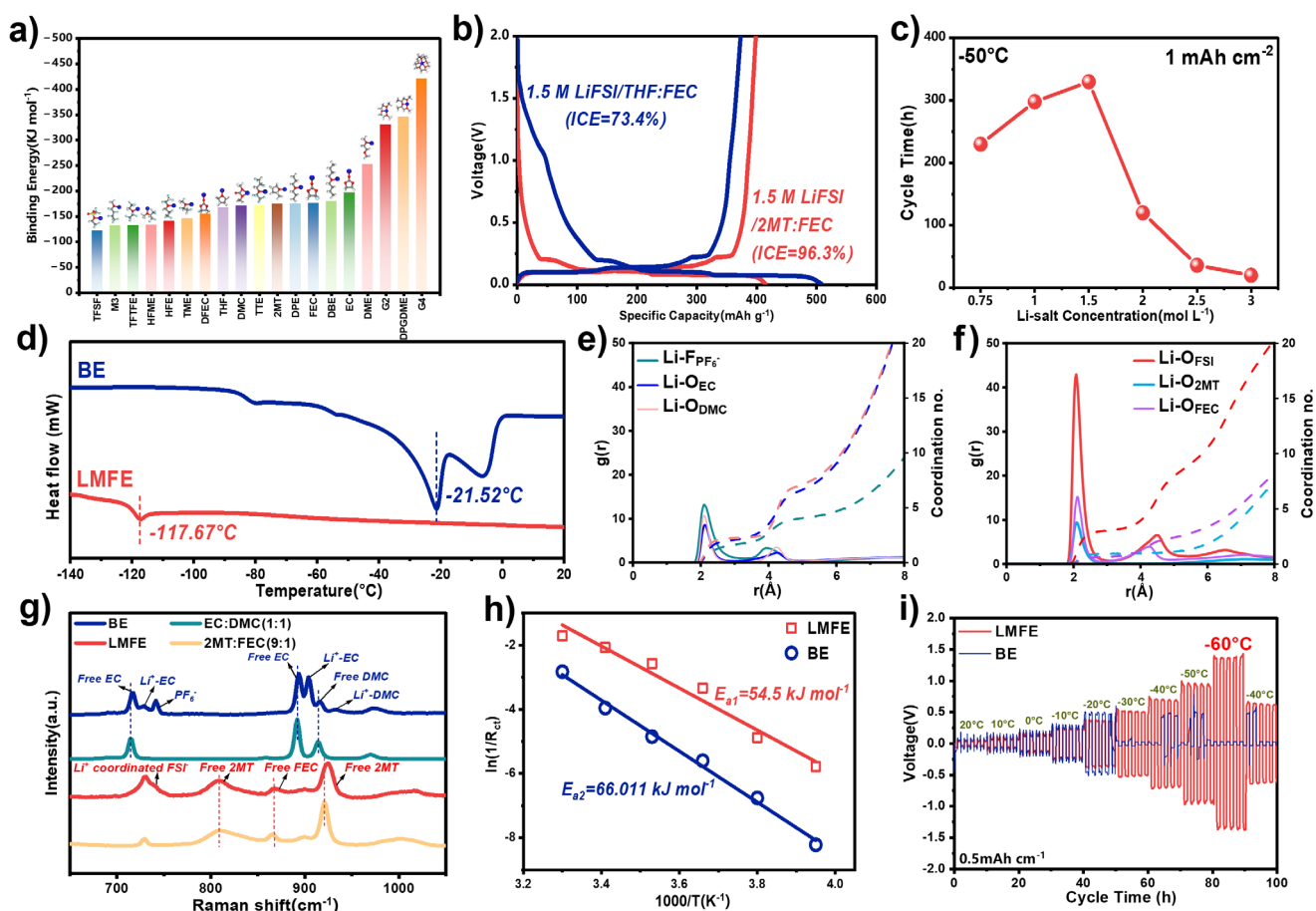
Figure 2. a) Binding energy (E_B) of Li$^+$ with various solvents obtained through DFT calculations. b) Initial charge–discharge curves of the Gr∥Li half-cells with the THF- and 2MT-based electrolytes at 0.1 C. c) Cycling performance of Li∥Li symmetric cells (1 mAh cm^{-2}) with various lithium salt concentrations at −50 °C. d) Differential scanning calorimetry (DSC) curves of the LMFE and BE electrolytes. e) Radial distribution function (RDF) curves from molecular dynamics (MD) simulations of the BE electrolytes. f) Radial distribution function (RDF) curves from MD simulations of the LMFE electrolytes. g) Raman spectra of solvents and electrolytes, showing the solvation structure of Li$^+$. h) Desolvation activation energies (E_a) of Li$^+$ in the LMFE and BE electrolytes. i) Cycling performance of Li∥Li symmetric cells with LMFE and BE at various temperatures.

and cryogenic performance of the 2MT-based electrolyte. Notably, control experiments with a FEC-free electrolyte (1.5 M LiFSI/2MT, LME) confirm that the weak solvation of 2MT is the primary driver for forming the protective LiF-rich SEI (primarily from LiFSI decomposition), while FEC serves a secondary role in further enhancing interfacial stability and fast-charging kinetics (Figures S7 and S8). Therefore, on the basis of the above design principles, a new WSE was proposed for low-temperature LIBs, with a composition of 1.5 M LiFSI /2MT:FEC (9:1 *v/v*) (LMFE), whereas the conventional carbonate electrolyte of 1 M LiPF$_6$/EC:DMC (1:1 *v/v*) was used as the baseline electrolyte (BE) for comparison.

The liquid range of these electrolytes was evaluated via differential scanning calorimetry (DSC) (Figure 2d). BE exhibited an endothermic peak at −21.52 °C, indicating a phase transition to a solid. In contrast, the LMFE demonstrated a significantly lower freezing point of −117.67 °C, reflecting its superior low-temperature fluidity. When stored at −60 °C for 2 h, the BE froze completely (Figure S9), whereas the LMFE remained liquid, highlighting its low-

temperature stability. Systematic rheological and conductivity analyses reveal LMFE's exceptional cryogenic fluidity, maintaining ultralow viscosity (17.8 mPa·s at −20 °C vs. 494.9 mPa·s for BE, Figure S10a,b) and measurable ionic conductivity down to −70 °C (1.42 mS cm^{-1}, Figure S10c). The 28-fold viscosity disparity at −20 °C and BE's solidification below −40 °C (aligned with DSC in Figure 2d) quantitatively explain LMFE's superior Li$^+$ transport. This synergy of weak solvation and depressed freezing point (−117.67 °C) enables unimpeded ion mobility across extreme temperatures, fulfilling critical electrolyte design criteria for LT operation. The radial distribution function (RDF) curves illustrate distinct differences in the solvation structures of the electrolytes. BE shows high Li$^+$-EC/DMC coordination numbers, indicating strong interactions between Li$^+$ and the carbonate molecules (Figures 2e and S11b). In contrast, the LMFE electrolyte shows a lower Li$^+$-2MT coordination number and a higher Li$^+$-FSI$^-$ coordination number, suggesting that FSI$^-$ anions predominantly occupy the Li$^+$ solvation shell and consequently decrease the involvement of solvent molecules in solvation (Figures 2f and S11a).

Raman spectroscopy confirmed such solvation structure (Figure 2g). The C—O—C ring-breathing mode of 2MT shifts from 920.4 to 922.5 cm^{-1} upon the addition of 1.5 M LiFSI without any new peak formation, indicating weak coordination between the Li$^+$ and 2MT molecules. The characteristic vibrational peak of LiFSI at 728.4 cm^{-1} remains dominant, highlighting the contribution of FSI− anions to Li$^+$ solvation. In the BE, the characteristic EC peaks at 714.1and 891.9 cm^{-1} (associated with free EC molecules) diminish significantly, while new peaks emerge at 729.5 and 905.3 cm^{-1}. These new peaks correspond to Li$^+$-coordinated EC species in contact ion pairs (CIPs) or aggregates (AGGs), confirming strong cation-solvent interactions. Additionally, a secondary peak at 933.7 cm^{-1} corresponds to Li$^+$-DMC coordination, suggesting moderate interaction with DMC molecules. These findings align with DFT calculations, which show that EC has a higher E_B with Li$^+$ (−197.61 kJ mol^{-1}) than 2MT does.

The desolvation activation energy (E_a) of Li$^+$ in LMFE is 54.5 kJ mol^{-1}, which is significantly lower than the 66.0 kJ mol^{-1} in BE (Figures 2h and S12). This indicates that LMFEs require less energy for Li$^+$ desolvation, facilitating faster ion transport at low temperatures. Additionally, the Li‖Li symmetric cell with LMFE maintains stable cycling from 20 °C to −60 °C due to its synergistic combination of low freezing point, maintained ion transport, reduced desolvation barriers, and stable interfacial chemistry. In contrast, the BE-based cell fails at −30 °C primarily due to electrolyte solidification. At −20 °C, the Li‖Li symmetric cell with LMFE exhibited a polarization of 351 mV, which was significantly lower than the polarization of 505 mV observed in the BE-based cell, confirming the limitations of commercial carbonate-based electrolytes in subzero environments (Figures 2i and S13).

Low-Temperature Performance of LFP‖Li Half Cells

The low-temperature behavior of LFP‖Li half-cells was systematically investigated with LMFE, BE, 1.5 M LiFSI/EC:DMC (1:1 *v/v*, LED), and 1.5 M LiFSI/EC:DMC:FEC (4.5:4.5:1 *v/v*, LEDF) electrolytes. As illustrated in Figure 3a, the LMFE-based cell exhibits exceptional rate capability at −10 °C, demonstrating stable cycling performance from 0.1 C to 2 C with a retained capacity of 116.9 mAh g^{-1}, corresponding to 78% of its room-temperature (RT) capacity. However, the low-temperature capacity of LED and LEDF reaches only 60% of LMFE's capacity. Even with the same LiFSI concentrations (1.5 M), their inferior performance confirms that the superiority arises from 2MT's weakly-solvated structure. Therefore, subsequent comparisons will focus on the differences between LMFE and BE electrolytes. The charge-discharge profiles in Figure 3b reveal that the LMFE-based cell has significantly lower polarization (141.8 mV) than the BE-based cell does (272.5 mV), indicating enhanced ionic transport and a reduction in interfacial resistance at subzero temperatures. Furthermore, as shown in Figure 3c, the LMFE-based cell maintains 96.4% capacity retention after 150 cycles

at −10 °C and 0.2C, accompanied by a high Coulombic efficiency of 99.97%. In stark contrast, the BE-based cell only achieves a capacity retention of 60.5%, underscoring the inherent limitations of carbonate-based electrolytes under low-temperature conditions.

Electrochemical impedance spectroscopy (EIS) demonstrated that the LFP‖Li half-cells exhibited significantly reduced impedance after three-cycle formation at RT, which was attributed to the formation of a stable solid-electrolyte interphase (SEI) layer and enhanced Li$^+$ ion transport (Figures 3d and S14). At −10 °C, the charge-transfer resistance (R_{ct}) of the BE-based cell increases substantially to 883.2 Ω (after 10 cycles) as the electrolyte approaches its freezing point, whereas the LMFE-based cell maintains superior ionic mobility with a much lower R_{ct} of 129.1 Ω (Figure 3e). Notably, the interfacial resistance (R_{SEI}) of the LMFE-based cell increases only marginally during the temperature transition, from 18.23 to 28.15 Ω, indicating the formation of a robust and conductive interfacial layer. The Nyquist plots confirm that R_{ct} represents the dominant impedance component in LFP‖Li cells, with significantly higher R_{ct} values being the primary limitation for BE-based cells under low-temperature conditions. Specifically, at − 10 °C, the R_{ct} of the BE is 6.32 times greater than its R_{SEI}, highlighting its inability to overcome the ionic transport challenges posed by subzero environments.

The low-temperature cycling stability of Li‖Li symmetric cells further demonstrates the advantages of LMFE (Figure 3f). The LMFE-based cell exhibited exceptional stability over a 1000 h test period at − 10 °C under a current density of 1 mA cm^{-2} and an areal capacity of 2 mAh cm^{-2}, whereas the BE-based cell failed prematurely after 360 h due to short-circuiting. Additionally, the LMFE-based cell displays superior reversibility and lower polarization, further underscoring its suitability for subzero-temperature applications.

Composition and Nanostructure of the Interphase

The enhanced reaction kinetic of LFP‖Gr full cells under both RT and low temperature (LT) conditions prompted an investigation into the interfacial evolution on Gr anodes. To directly correlate SEI properties with full-cell behavior, Gr electrodes were systematically characterized under three operational scenarios: after formation cycling at RT, after 20 cycles at −10 °C, and at high rate of 5C (RT). XPS analysis revealed that after formation cycles, the SEI on graphite in LMFE exhibits a higher LiF content of 25.4% (F*1s* peak at 685.1 eV) compared to 20.5% in BE (Figure 4d,g). Concurrently, organic components (e.g., ROCO$_2$Li, C *1s* peak at 289.5 eV) are slightly reduced in LMFE (15.8% *vs*. 19.3% in BE), indicating suppressed solvent decomposition (Figure 4a,g). While the initial SEI differences are modest, they establish a foundation for divergent interfacial evolution under harsh conditions. The organic SEI component primarily arises from the electrochemical reduction of EC.[34] After 20 cycles at −10 °C, the SEI disparity amplifies significantly. In LMFE, LiF content remains high at 20.0%, whereas
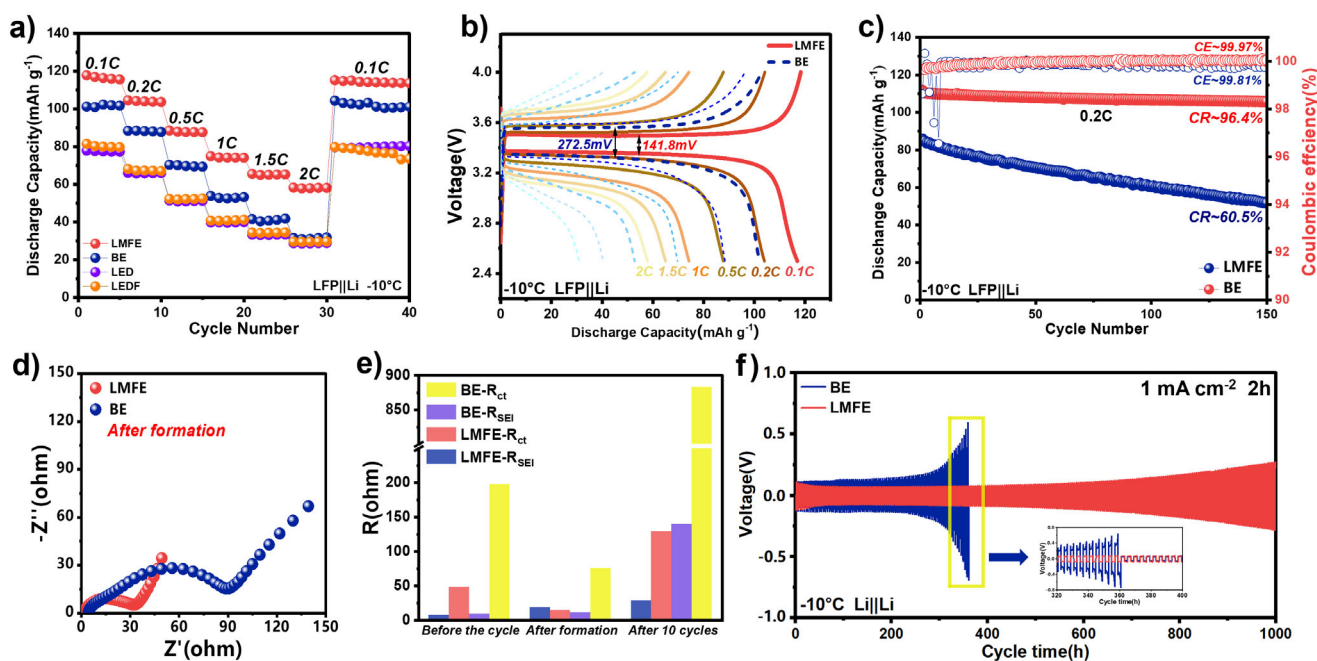
Figure 3. a) Rate capability of LFP||Li half-cells with LMFE and BE at −10 °C. b) Charge–discharge curves of LFP||Li half-cells with LMFE and BE at −10 °C. c) Cycling performance of LFP||Li half-cells at −10 °C and 0.2 C in LMFE and BE electrolytes. d) EIS of LFP||Li half-cells after RT formation. e) Fitted R_{SEI} and R_{ct} values for LMFE- and BE-based cells. f) Cycling performance of Li||Li symmetric cells at −10 °C at a current density of 1 mA cm^{-2} and an areal capacity of 2 mAh cm^{-2}.

BE's LiF drops to 14.1% (Figure 4b,g). The excellent electronic insulation of LiF effectively suppresses electron tunneling, contributing to high electrochemical stability and a wide electrochemical window. Moreover, LiF can induce Li lateral dispersion and thus inhibit the growth of vertical dendrites due to high interfacial energy.[35–37] Organic species (ROCO$_2$Li) in LMFE are reduced to 7.0%, threefold lower than BE's 20.5% (Figure 4e,g). This inorganics-dominated SEI in LMFE, with its high ionic conductivity, minimizes interfacial resistance and sustains Li$^+$ transport at LT. Under 5C charging, LMFE's SEI becomes overwhelmingly inorganic, with LiF content reaching 49.1% (Figure 4f,g), far exceeding BE's 14.5%. Organic components (ROCO$_2$Li) in LMFE are suppressed to 6.5% (*vs.* 22.3% in BE) (Figure 4c,g). The LiF-rich SEI reduces charge-transfer resistance enabling rapid Li$^+$ intercalation/deintercalation.[38]

The cryo-TEM and Fast Fourier Transform (FFT) analyses reveal substantially different SEI nanostructures: In LMFE, the SEI is thinner (13 nm *vs.* 26 nm in BE) and exhibits more uniform thickness (Figure 5a–c, Figures S15–S17), consisting primarily of inorganic species including LiF, Li$_2$O,Li$_2$CO$_3$, and Li$_3$N nanocrystals embedded in a minimal organic matrix.[39–44] Inorganic species such as LiF/Li$_2$O/Li$_3$N are mainly derived from FSI− decomposition.[45] This observation aligns perfectly with XPS results showing inorganics-dominated SEI composition. The thinner SEI in the LMFE facilitates Li$^+$ transport by reducing the ionic migration distance, whereas the abundant grain boundaries formed by Li$_2$O/LiF/Li$_3$N/Li$_2$CO$_3$ within the SEI significantly increase its ionic conductivity.[38,46] In contrast, BE forms a thicker, highly heterogeneous SEI (Figure 5d–f) dominated by amor-

phous components with only sporadic LiF and Li$_2$CO$_3$ nanograins, consistent with incomplete electrolyte decomposition at low temperatures.[47,48] This interphase impedes Li$^+$ transport, contributing to the poor low-temperature performance of BE cells. The comparative EELS analysis of the C *K*-edge and O *K*-edge spectra definitively confirmed the predominantly organic character of the BE-derived SEI, in stark contrast to the inorganic-rich LMFE SEI (Figure S18). The agreement between the measured and theoretical interplanar spacings of the identified inorganic phases (discrepancies < 0.5%), as statistically summarized in Table S3, provides robust crystallographic evidence for our phase assignments. Calendar aging tests at −10 °C reveal drastically divergent stability: BE suffers linear capacity fade (2.0 mAh g^{-1} per 48 h), while LMFE retains 99.92% capacity over 192 h (Figure S19). This resilience directly stems from LMFE's inorganics-rich SEI (Figure 5a–c), which effectively suppresses electrolyte decomposition and lithium depletion under cryogenic conditions—validating its dual functionality for both cycling and long-term storage in extreme environments.

Similar inorganics-rich interphases were formed on the Li metal anode (Figures S20 and S21), which is beneficial for achieving dense Li deposits. Cross-sectional SEM reveals that BE induces heterogeneous lithium deposits with dendritic protrusions and porous structures (*avg.* thickness: 35.0 μm, Figure S22a–d), exacerbated by sluggish kinetics. Conversely, LMFE achieves uniform, dense Li deposition with a thickness of 6.4 μm—5.5 times thinner than BE (Figure S22e,f). At RT, LMFEs achieve uniform lithium deposition (Figure S23a), whereas at −10 °C, smaller lithium particles with slight
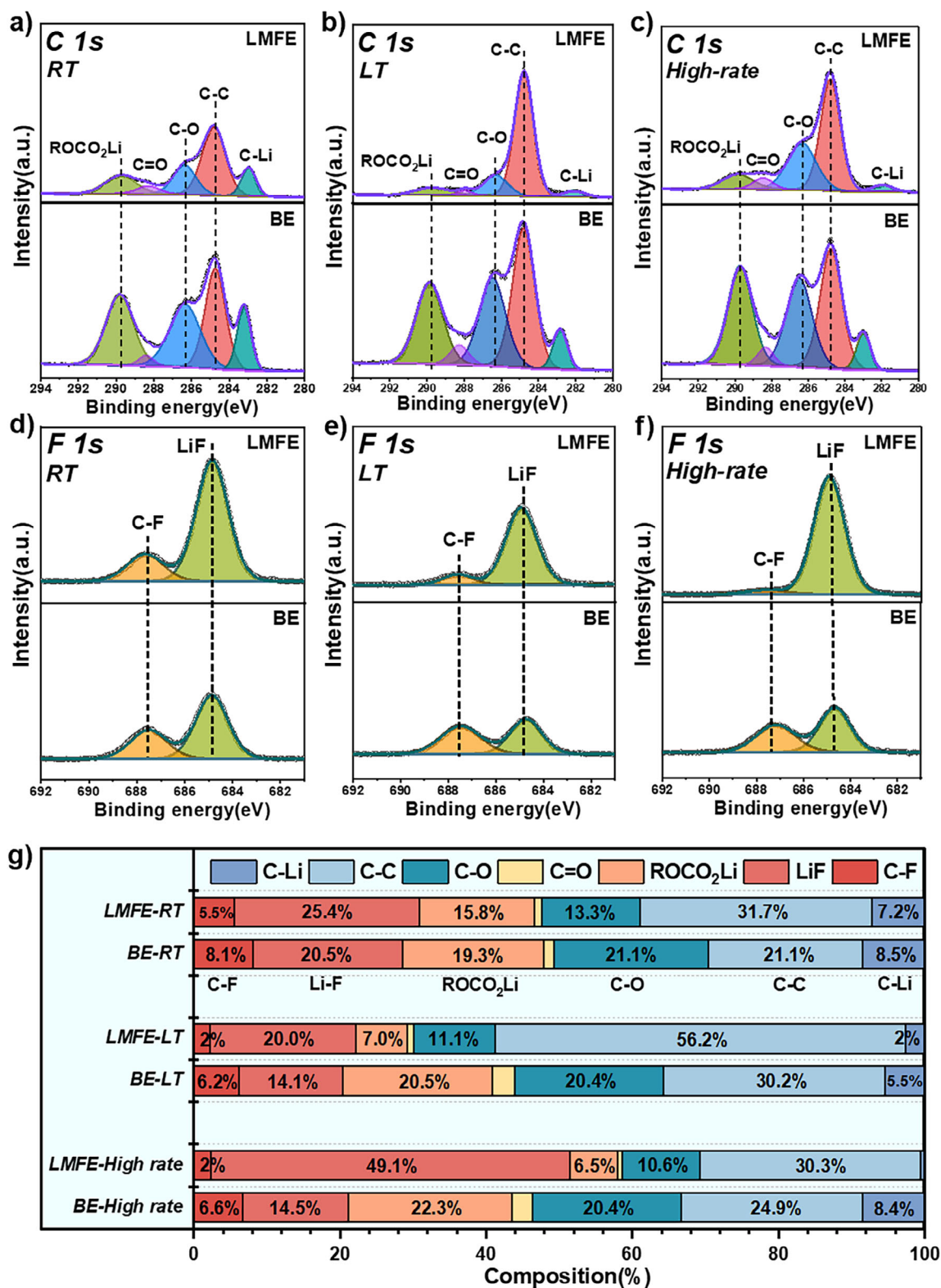
Figure 4. a) C 1s spectra of the SEI on the Gr anodes after formation (three cycles at RT and 0.2C). b) C 1s spectra of the SEI on the Gr anodes after 20 cycles at − 10 °C and 0.1 C. c) C 1s spectra of the SEI on the Gr anodes after 20 cycles at RT and 5C. d) F 1s spectra of the SEI on the Gr anodes after formation (three cycles at RT and 0.2C). e) F 1s spectra of the SEI on the Gr anodes after 20 cycles at − 10 °C and 0.1 C. f) F 1s spectra of the SEI on the Gr anodes after 20 cycles at RT and 5C. g) Quantitative comparison of the SEI composition formed in different electrolytes by XPS analysis.
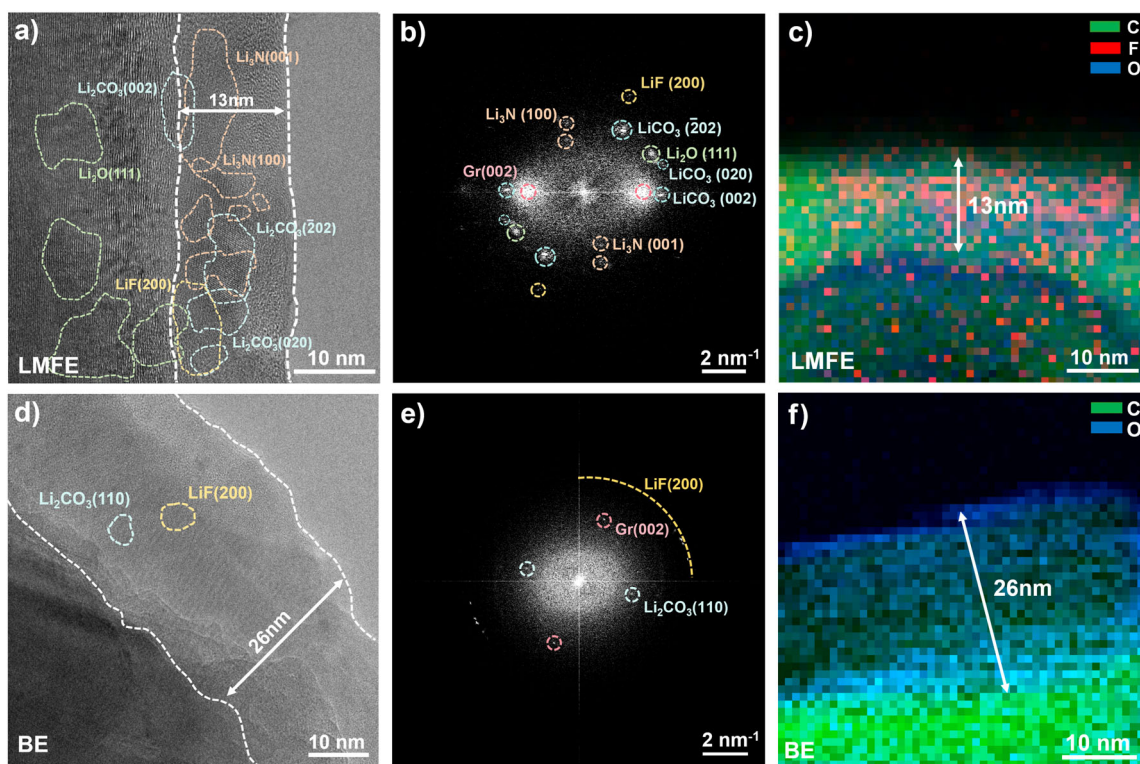
Angew. Chem. Int. Ed. **2025**, e21171 (6 of 10)

© 2025 Wiley-VCH GmbH

Figure 5. a) and d) Cryo-TEM images, b) and e) Corresponding FFT patterns, and c) and f) Electron energy loss spectroscopy (EELS) mapping of the SEI of Gr anodes cycled in LMFE and BE at 0.2C and −10 °C for 20 cycles.

whisker-like structures are observed (Figure S23b). In contrast, the BE exhibited abundant whisker-like lithium structures at RT (Figure S23c), which further deteriorated into needle-like dendrites as the temperature decreased (Figure S23d). This unfavorable deposition accelerates electrolyte consumption, promotes the formation of "dead lithium", and correlates with the poor electrochemical performance of BE at −10 °C. Moreover, needle-like dendrites pose a significant risk of separator piercing, increasing the likelihood of short circuits.

Fast-Charging Capability and Low-Temperature Performance

The low temperature and fast-charging performance of LFMEs was systematically evaluated, with a particular focus on their long-term cycling stability at −30 °C and high-rate charging capability—both critical metrics for power battery applications. As illustrated in Figure 6a, LFP‖Li half-cells employing LMFE retain 93.83% of their initial capacity after 150 cycles at −30 °C and 0.1 C, accompanied by a Coulombic efficiency of 99.97%. This demonstrates exceptional capacity retention and Coulombic efficiency at ultralow temperatures. The fast-charging capability of LMFEs is further emphasized in Figure 6b, where LFP‖Li cells utilizing LMFEs retained five times the capacity of BE cells at a 5 C charge rate. At RT, LMFEs achieve 82.4% capacity retention after 350 cycles at 1 C, significantly surpassing the BE performance of 30.3% (Figure S24a).

The electrochemical performance of the Li‖Gr half-cells was also assessed at both RT and −30 °C. At 1 C, the LMFE delivers a high capacity of 366 mAh g^{-1}, closely approaching the theoretical capacity of Gr (372 mAh g^{-1}) (Figure S24b). Even at an elevated rate of 5C, LMFE achieves a reversible capacity of 288.4 mAh g^{-1}, corresponding to a retention rate of 77%. When subjected to a 7 C charge rate, the capacity remains at 162.8 mAh g^{-1}, significantly exceeding the BE capacity of 86.90 mAh g^{-1} at 5C (Figure 6d). Furthermore, LMFEs facilitate excellent cycling stability for Gr anodes, achieving a Coulombic efficiency close to 100% and retaining 95.74% of their initial capacity after 500 cycles at 1C (Figure S24b). These results underscore the outstanding fast-charging capability and long-term cycling stability of LMFEs, rendering them highly suitable for high-rate applications with Gr anodes.

Gr anodes face significant challenges at low temperatures because of the high overpotential associated with sluggish desolvation kinetics and poor ion transport through the SEI, often resulting in severe capacity loss or inability to intercalate Li$^+$ during charging. However, the optimized design of LMFEs successfully addresses these limitations, enabling a reversible capacity of 244 mAh g^{-1} at −30 °C, equivalent to 67% of its RT capacity—a notable achievement for Gr anodes. Even after 180 cycles at −30 °C, the Gr‖Li half-cells with LMFEs retain an impressive capacity of 96.33%, accompanied by a Coulombic efficiency of 98.31% (Figures 6c and S25). This remarkable performance highlights the efficient desolvation process and robust SEI structure of LMFEs,
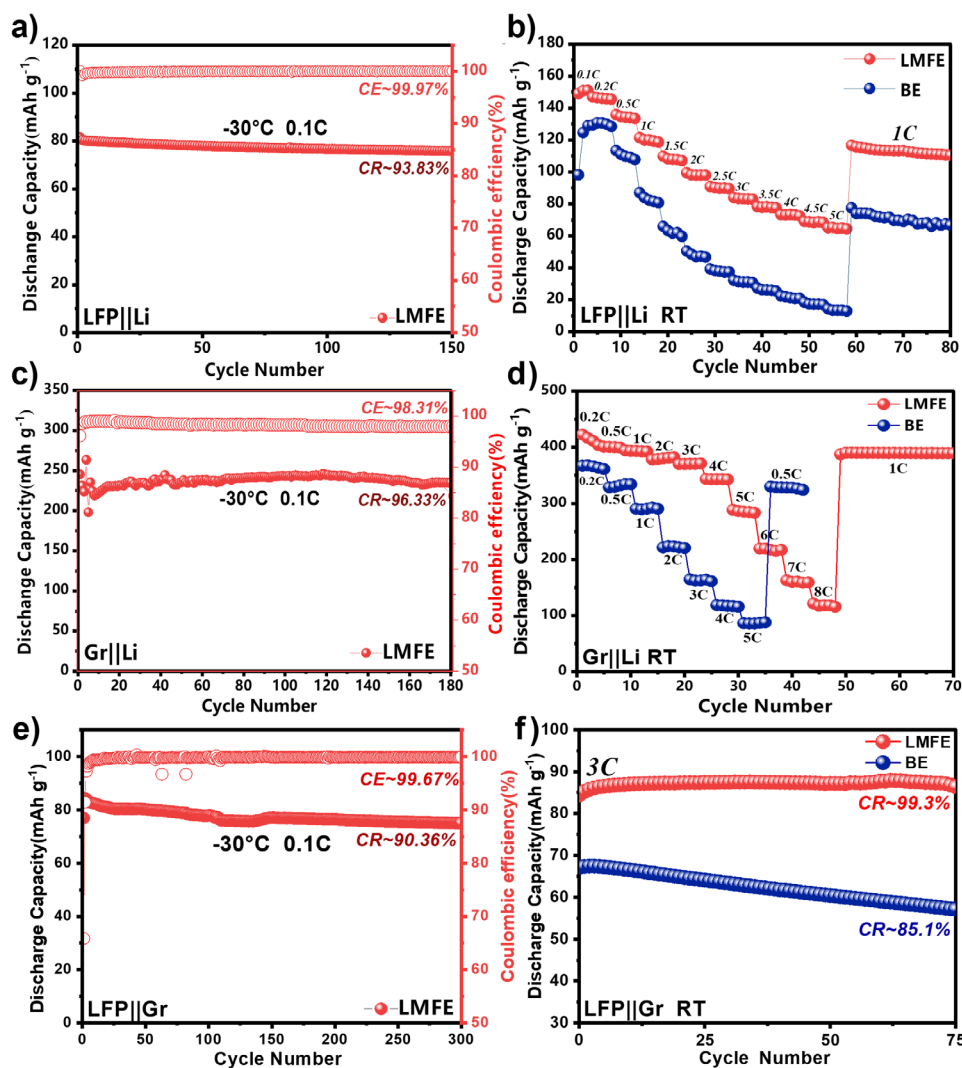
Figure 6. a) Cycling performance of LFP||Li half-cells in LMFE at −30 °C and 0.1 C. b) Rate capability of LFP||Li half-cells in LMFE and BE at RT. c) Cycling performance of the Gr||Li half-cells in LMFE at −30 °C and 0.1 C. d) Rate performances of the Gr||Li half-cells in the LMFE and BE at RT. e) Cycling performance of LFP||Gr cells in LMFE at −30 °C and 0.1 C. f) Comparative cycling performance of LFP||Gr full cells in LMFE and BE at RT and 3 C.

which collectively support their superior low-temperature functionality.

Finally, the long-term cycling stability and temperature adaptability of LFP||Gr full cells further validate the potential of LMFEs for extreme conditions (Figure 6e). At −30 °C, the LMFE retains 90.36% of its capacity after 300 cycles, with a Coulombic efficiency of 99.67%. To further substantiate the fast-charging capability under extreme conditions, the LFP||Gr full cell was subjected to long-term cycling at a high rate of 3C. Remarkably, the cell retains 99.3% of its capacity after 75 cycles (Figure 6f), significantly outperforming the baseline electrolyte (85.1%). At an even higher rate of 5C, the LMFE-based full cell delivers a specific capacity that is 21.7% greater than that of the BE-based cell, further demonstrating its superior fast-charging capability 7(Figure S26). A performance comparison with recently reported state-of-the-art electrolytes (Table S4) confirms the competitiveness of our LMFE formulation, particularly in balancing low-temperature operation and fast-charging capability. To explore the temperature limitations of LMFEs, Li||Li symmetric cells were tested. As shown in Figure S27, LMFE enables stable cycling for more than 1600 h at −30 °C and maintains consistent performance at −50 °C for more than 300 h. Even at −60 °C, LMFE exhibited remarkable cycling stability (Figure 2i). These results demonstrate the superiority of LMFEs over conventional carbonate-based electrolytes, offering a reliable solution for low-temperature battery applications.

Conclusion

In this study, we introduced a weakly solvating electrolyte (LMFE) based on 2-methyl-tetrahydrofuran (2MT) and fluoroethylene carbonate (FEC), which is specifically designed to overcome the limitations of traditional electrolytes in terms of

low-temperature performance and fast-charging applications for lithium-ion batteries (LIBs). The optimized composition of LMFE exhibited remarkable low-temperature stability, maintaining liquidity at temperatures as low as $-117\,°C$ while ensuring high ionic conductivity and enhanced interfacial lithium-ion transport. The experimental results highlight the superior performance of LMFEs compared with that of conventional carbonate-based electrolytes. In the Gr‖Li half-cells, the LMFE achieves a reversible capacity of 366 mAh g^{-1} at $-30\,°C$ with a Coulombic efficiency of 96.3% and retains 67% of its RT capacity at $-30\,°C$. This underscores the exceptional fast-charging capability and robust low-temperature functionality of LMFEs. Furthermore, the LMFE enables stable cycling in Li‖Li symmetric cells for over 1600 h at $-30\,°C$ and more than 300 h at $-50\,°C$, demonstrating its adaptability across a wide temperature range. The advanced SEI structure formed by LMFEs, which are rich in inorganic components such as LiF, Li_3N, Li_2CO_3 and Li_2O, contributes to their stable cycling performance by reducing the desolvation energy and improving the ionic conductivity. In LFP‖Gr full cells, the LMFE retains 90.36% of its initial capacity after 300 cycles at $-30\,°C$, with a Coulombic efficiency of 99.67%, further demonstrating its capacity retention and long-term stability at ultralow temperatures. In conclusion, LMFEs offer a transformative solution for next-generation LIBs by addressing the critical challenges of fast-charging and low-temperature operation without compromising cycling stability. Its ability to perform efficiently across extreme temperature ranges makes LMFE a promising candidate for future energy storage technologies, particularly in applications demanding high reliability in harsh environments, such as electric vehicles, aerospace, and military equipment.

Supporting Information

The authors have cited additional references within the Supporting Information.

Acknowledgements

Conflict of Interests

The authors declare no conflict of interest.

Data Availability Statement

The data that support the findings of this study are available from the corresponding author upon reasonable request.

[1] H. Zhang, C. Li, G. G. Eshetu, S. Laruelle, S. Grugeon, K. Zaghib, C. Julien, A. Mauger, D. Guyomard, T. Rojo, N. Gisbert-Trejo, S. Passerini, X. Huang, Z. Zhou, P. Johansson, M. Forsyth, *Angew. Chem. Int. Ed.* **2020**, *59*, 534–538, https://doi.org/10.1002/anie.201913923.

[2] J. Xiao, F. Shi, T. Glossmann, C. Burnett, Z. Liu, *Nat. Energy* **2023**, *8*, 329–339, https://doi.org/10.1038/s41560-023-01221-y.

[3] R. Schmuch, R. Wagner, G. Hörpel, T. Placke, M. Winter, *Nat. Energy* **2018**, *3*, 267–278, https://doi.org/10.1038/s41560-018-0107-2.

[4] Y. Shi, X. Chen, T. Jiang, Q. Jin, *Sustainable Production and Consumption* **2023**, *35*, 525–538, https://doi.org/10.1016/j.spc.2022.11.021.

[5] Z. Li, Y. X. Yao, M. Zheng, S. Sun, Y. Yang, Y. Xiao, L. Xu, C. B. Jin, X. Y. Yue, T. Song, P. Wu, C. Yan, Q. Zhang, *Angew. Chem. Int. Ed.* **2024**, e202409409, https://doi.org/10.1002/ange.202409409.

[6] J. Xue, Z. Zhang, Y. Wang, J. Lin, Q. Fu, G. Liang, *J. Alloys Compd.* **2025**, *1010*, 177698, https://doi.org/10.1016/j.jallcom.2024.177698.

[7] L. Dong, H. J. Yan, Q. X. Liu, J. Y. Liang, J. Yue, M. Niu, X. Chen, E. Wang, S. Xin, X. Zhang, C. Yang, Y. G. Guo, *Angew. Chem. Int. Ed.* **2024**, *63*, e202411029, https://doi.org/10.1002/anie.202411029.

[8] K. Yan, J. Wang, S. Zhao, D. Zhou, B. Sun, Y. Cui, G. Wang, *Angew. Chem. Int. Ed.* **2019**, *58*, 11364–11368, https://doi.org/10.1002/anie.201905251.

[9] Y. Gao, T. Rojas, K. Wang, S. Liu, D. Wang, T. Chen, H. Wang, A. T. Ngo, D. Wang, *Nat. Energy* **2020**, *5*, 534–542, https://doi.org/10.1038/s41560-020-0640-7.

[10] L. Chen, B. Xiao, W. Chen, P. Zhang, T. Huang, W. Huang, Z. Huang, Q. Lin, P. Liu, X. He, Y. Liu, H. Wei, S. Ye, L. Li, J. Chen, X. Yang, X. Ren, X. Ouyang, J. Liu, F. Pan, Q. Zhang, J. Hu, *Nano Energy* **2024**, *131*, 110276, https://doi.org/10.1016/j.nanoen.2024.110276.

[11] J. F. Gohy, S. Yan, J. Liu, Z. He, H. Jia, Z. Chen, Y. Zhang, *Angew. Chem. Int. Ed.* **2025**, e202503307, https://doi.org/10.1016/j.nanoen.2024.110276.

[12] J. S. Menye, M.-B. Camara, B. Dakyo, *Energies.* **2025**, *18*, 342, https://doi.org/10.3390/en18020342.

[13] N. Zhang, T. Deng, S. Zhang, C. Wang, L. Chen, C. Wang, X. Fan, *Adv. Mater.* **2022**, *34*, 2107899, https://doi.org/10.1002/adma.202107899;

[14] C. Yan, Y.-X. Yao, W.-L. Cai, L. Xu, S. Kaskel, H. S. Park, J.-Q. Huang, *J. Energy Chem.* **2020**, *49*, 335–338, https://doi.org/10.1016/j.jechem.2020.02.052.

[15] G. Wang, G. Wang, L. Fei, L. Zhao, H. Zhang, *Nano-Micro Lett.* **2024**, *16*, 150, https://doi.org/10.1007/s40820-024-01363-y.

[16] Q. Li, G. Liu, H. Cheng, Q. Sun, J. Zhang, J. Ming, *Chemistry.* **2021**, *27*, 15842–15865, https://doi.org/10.1002/chem.202101407

[17] A. Gupta, A. Manthiram, *Adv. Energy Mater.* **2020**, *10*, 2001972, https://doi.org/10.1002/aenm.202001972.

[18] Y. X. Yao, X. Chen, N. Yao, J. H. Gao, G. Xu, J. F. Ding, C. L. Song, W. L. Cai, C. Yan, Q. Zhang, *Angew. Chem. Int. Ed.* **2023**, *62*, e202214828, https://doi.org/10.1002/anie.202214828.

[19] L. Xu, Y. Xiao, Y. Yang, S. J. Yang, X. R. Chen, R. Xu, Y. X. Yao, W. L. Cai, C. Yan, J. Q. Huang, Q. Zhang, *Angew. Chem. Int. Ed.* **2022**, *61*, e202210365, https://doi.org/10.1002/anie.202210365;

[20] J. Xu, J. Zhang, T. P. Pollard, Q. Li, S. Tan, S. Hou, H. Wan, F. Chen, H. He, E. Hu, K. Xu, X.-Q. Yang, O. Borodin, C. Wang, *Nature* **2023**, *614*, 694–700, https://doi.org/10.1038/s41586-022-05627-8.

[21] B. Han, Y. Zou, G. Xu, S. Hu, Y. Kang, Y. Qian, J. Wu, X. Ma, J. Yao, T. Li, Z. Zhang, H. Meng, H. Wang, Y. Deng, J. Li, M. Gu, *Energy Environ. Sci.* **2021**, *14*, 4882–4889, https://doi.org/10.1039/D1EE01678D.

[22] J. Hou, M. Yang, D. Wang, J. Zhang, *Adv. Energy Mater.* **2020**, *10*, 1904152, https://doi.org/10.1002/aenm.201904152.

[23] K. Xu, *Chem. Rev.* **2004**, *104*, 4303–4418, https://doi.org/10.1021/cr030203g.

[24] D. Hubble, D. E. Brown, Y. Zhao, C. Fang, J. Lau, B. D. McCloskey, G. Liu, *Energy Environ. Sci.* **2022**, *15*, 550–578, https://doi.org/10.1039/D1EE01789F.

[25] Y.-X. Yao, N. Yao, X.-R. Zhou, Z.-H. Li, X.-Y. Yue, C. Yan, Q. Zhang, *Adv. Mater.* **2022**, *34*, 2206448, https://doi.org/10.1002/adma.202206448.

[26] A. Huang, Z. Ma, P. Kumar, H. Liang, T. Cai, F. Zhao, Z. Cao, L. Cavallo, Q. Li, J. Ming, *Nano Lett.* **2024**, *24*, 7499–7507, https://doi.org/10.1021/acs.nanolett.4c01591.

[27] P. Ma, P. Mirmira, P. J. Eng, S.-B. Son, I. D. Bloom, A. S. Filatov, C. V. Amanchukwu, *Energy Environ. Sci.* **2022**, *15*, 4823–4835, https://doi.org/10.1039/D2EE01489K.

[28] W. Wahyudi, V. Ladelta, L. Tsetseris, M. M. Alsabban, X. Guo, E. Yengel, H. Faber, B. Adilbekova, A. Seitkhan, A. H. Emwas, M. N. Hedhili, L. J. Li, V. Tung, N. Hadjichristidis, T. D. Anthopoulos, J. Ming, *Adv. Funct. Mater.* **2021**, *31*, 2101593, https://doi.org/10.1002/adfm.202101593;

[29] S. Maruyama, T. Fukutsuka, K. Miyazaki, T. Abe, *J. Appl. Electrochem.* **2019**, *49*, 639–646, https://doi.org/10.1007/s10800-019-01312-3.

[30] M. Qin, Z. Zeng, Q. Wu, H. Yan, M. Liu, Y. Wu, H. Zhang, S. Lei, S. Cheng, J. Xie, *Energy Environ. Sci.* **2023**, *16*, 546–556, https://doi.org/10.1039/D2EE03626F

[31] H. Zhang, Z. Zeng, F. Ma, Q. Wu, X. Wang, S. Cheng, J. Xie, *Angew Chem. Int. Ed.* **2023**, *62*, e202300771, https://doi.org/10.1002/anie.202300771.

[32] J. Chen, X. Fan, Q. Li, H. Yang, M. R. Khoshi, Y. Xu, S. Hwang, L. Chen, X. Ji, C. Yang, H. He, C. Wang, E. Garfunkel, D. Su, O. Borodin, C. Wang, *Nat. Energy* **2020**, *5*, 386–397, https://doi.org/10.1038/s41560-020-0601-1.

[33] J. F. Leal Silva, A. P. Mariano, R. Maciel Filho, *Biomass Bioenergy* **2018**, *119*, 492–502, https://doi.org/10.1016/j.biombioe.2018.10.008.

[34] L. Wang, A. Menakath, F. Han, Y. Wang, P. Y. Zavalij, K. J. Gaskell, O. Borodin, D. Iuga, S. P. Brown, C. Wang, K. Xu, B. W. Eichhorn, *Nat. Chem.* **2019**, *11*, 789–796, https://doi.org/10.1038/s41557-019-0304-z.

[35] P. Liu, H. Su, Y. Liu, Y. Zhong, C. Xian, Y. Zhang, X. Wang, X. Xia, J. Tu, *Small Struct.* **2022**, *3*, 2200010, https://doi.org/10.1002/sstr.202200010;

[36] S. Liu, X. Ji, J. Yue, S. Hou, P. Wang, C. Cui, J. Chen, B. Shao, J. Li, F. Han, J. Tu, C. Wang, *J. Am. Chem. Soc.* **2020**, *142*, 2438–2447, https://doi.org/10.1021/jacs.9b11750.

[37] Y. Wang, F. Liu, G. Fan, X. Qiu, J. Liu, Z. Yan, K. Zhang, F. Cheng, J. Chen, *J. Am. Chem. Soc.* **2021**, *143*, 2829–2837, https://doi.org/10.1021/jacs.0c12051.

[38] J. Tan, J. Matz, P. Dong, J. Shen, M. Ye, *Adv. Energy Mater.* **2021**, *11*, 2100046, https://doi.org/10.1002/aenm.202100046.

[39] Z. Li, Z. Chen, N. Sun, D. Wang, X. Yao, Z. Peng, *Angew Chem. Int. Ed.* **2024**, *63*, e202400876, https://doi.org/10.1002/anie.202400876.

[40] X. Zhou, F. Huang, X. Zhang, B. Zhang, Y. Cui, Z. Wang, Q. Yang, Z. Ma, J. Liu, *Angew Chem. Int. Ed.* **2024**, *63*, e202401576, https://doi.org/10.1002/anie.202401576.

[41] Y. Li, F. Bai, C. Li, Y. Wang, T. Li, *Adv. Energy Mater.* **2024**, *14*, 2304414, https://doi.org/10.1002/aenm.202304414.

[42] P. Lai, Y. Zhang, B. Huang, X. Deng, H. Hua, Q. Chen, S. Zhao, J. Dai, P. Zhang, J. Zhao, *Energy Storage Mater.* **2024**, *67*, 103314, https://doi.org/10.1016/j.ensm.2024.103314.

[43] Y. Jie, S. Wang, S. Weng, Y. Liu, M. Yang, C. Tang, X. Li, Z. Zhang, Y. Zhang, Y. Chen, F. Huang, Y. Xu, W. Li, Y. Guo, Z. He, X. Ren, Y. Lu, K. Yang, S. Cao, H. Lin, R. Cao, P. Yan, T. Cheng, X. Wang, S. Jiao, D. Xu, *Nat. Energy* **2024**, *9*, 987–998, https://doi.org/10.1038/s41560-024-01565-z.

[44] J. Yang, M. Li, Z. Sun, X. Lian, Y. Wang, Y. Niu, C. Jiang, Y. Luo, Y. Liu, Z. Tian, Y. Long, K. Zhang, P. Yu, J. Zhang, Z. Wang, G. Wu, M. Gu, W. Chen, *Energy Environ. Sci.* **2023**, *16*, 3837–3846, https://doi.org/10.1039/D3EE00161J.

[45] W. Yu, K. Y. Lin, D. T. Boyle, M. T. Tang, Y. Cui, Y. Chen, Z. Yu, R. Xu, Y. Lin, G. Feng, Z. Huang, L. Michalek, W. Li, S. J. Harris, J. C. Jiang, F. Abild-Pedersen, J. Qin, Y. Cui, Z. Bao, *Nat. Chem.* **2025**, *17*, 246–255, https://doi.org/10.1038/s41557-024-01689-5.

[46] X.-X. Ma, X. Shen, X. Chen, Z.-H. Fu, N. Yao, R. Zhang, Q. Zhang, *Small Struct.* **2022**, *3*, 2200071, https://doi.org/10.1002/sstr.202200071.

[47] S. Weng, X. Zhang, G. Yang, S. Zhang, B. Ma, Q. Liu, Y. Liu, C. Peng, H. Chen, H. Yu, X. Fan, T. Cheng, L. Chen, Y. Li, Z. Wang, X. Wang, *Nat. Commun.* **2023**, *14*, 4474, https://doi.org/10.1038/s41467-023-40221-0.

[48] Q. Zhao, S. Stalin, L. A. Archer, *Joule.* **2021**, *5*, 1119–1142, https://doi.org/10.1016/j.joule.2021.03.024.